

RESEARCH ARTICLE

# 3D-printed biodegradable magnesium alloy scaffolds with zoledronic acid-loaded ceramic composite coating promote osteoporotic bone defect repair

Zhaoyang Ran<sup>1,2†</sup>, Yan Wang<sup>3†</sup>, Jiaxin Li<sup>4†</sup>, Wenyu Xu<sup>5</sup>, Jia Tan<sup>1,2</sup>, Bojun Cao<sup>1,2</sup>, Dinghao Luo<sup>1,2</sup>, Yiwen Ding<sup>5</sup>, Junxiang Wu<sup>1,2</sup>, Lei Wang<sup>1,2</sup>, Kai Xie<sup>1,2</sup>, Liang Deng<sup>1,2</sup>, Penghuai Fu<sup>5\*</sup>, Xiaoying Sun<sup>3\*</sup>, Liyi Shi<sup>3</sup>, Yongqiang Hao<sup>1,2\*</sup>

<sup>1</sup>Shanghai Key Laboratory of Orthopaedic Implants, Department of Orthopaedic Surgery, Shanghai Ninth People's Hospital, Shanghai Jiao Tong University School of Medicine, Shanghai 200011, China

<sup>2</sup>Shanghai Engineering Research Center of Innovative Orthopaedic Instruments and Personalized Medicine, Shanghai Ninth People's Hospital, Shanghai Jiao Tong University School of Medicine, Shanghai 200011, China

<sup>3</sup>Nano-Science & Technology Center, College of Sciences, Shanghai University, Shanghai 200444, China

<sup>4</sup>Department of Orthopedics, The Second Affiliated Hospital of Harbin Medical University, Harbin 150001, China

<sup>5</sup>National Engineering Research Center of Light Alloy Net Forming & State Key Laboratory of Metal Matrix Composite, Shanghai Jiao Tong University, Shanghai 200240, China

†These authors contributed equally to this work.

**\*Corresponding authors:**

Yongqiang Hao  
(hyq\_9hospital@hotmail.com)

Xiaoying Sun  
(xysun@shu.edu.cn)

Penghuai Fu  
(fph112sjtu@sjtu.edu.cn)

**Citation:** Ran Z, Wang Y, Li J, *et al.*, 2023, 3D-printed biodegradable magnesium alloy scaffolds with zoledronic acid-loaded ceramic composite coating promote osteoporotic bone defect repair. *Int J Bioprint*, 9(5): 769. <https://doi.org/10.18063/ijb.769>

**Received:** March 19, 2023

**Accepted:** April 27, 2023

**Published Online:** June 7, 2023

**Copyright:** © 2023 Author(s). This is an Open Access article distributed under the terms of the Creative Commons Attribution License, permitting distribution, and reproduction in any medium, provided the original work is properly cited.

**Publisher's Note:** Whioce Publishing remains neutral with regard to jurisdictional claims in published maps and institutional affiliations.

This article has been updated with modifications. See the correction notice (doi: 10.36922/ijb.corr051826).

## Abstract

Osteoporotic fracture is one of the most serious complications of osteoporosis. Most fracture sites have bone defects, and restoring the balance between local osteogenesis and bone destruction is difficult during the repair of osteoporotic bone defects. In this study, we successfully fabricated three-dimensional (3D)-printed biodegradable magnesium alloy (Mg-Nd-Zn-Zr) scaffolds and prepared a zoledronic acid-loaded ceramic composite coating on the surface of the scaffolds. The osteogenic effect of Mg and the osteoclast inhibition effect of zoledronic acid were combined to promote osteoporotic bone defect repair. *In vitro* degradation and drug release experiments showed that the coating significantly reduced the degradation rate of 3D-printed Mg alloy scaffolds and achieved a slow release of loaded drugs. The degradation products of drug-loaded coating scaffolds can promote osteogenic differentiation of bone marrow mesenchymal stem cells as well as inhibit the formation of osteoclasts and the bone resorption by regulating the expression of related genes. Compared with the uncoated scaffolds, the drug-coated scaffolds degraded at a slower rate, and more new bone grew into these scaffolds. The healing rate and quality of the osteoporotic bone defects significantly improved in the drug-coated scaffold group. This study provides a new method for theoretical research and clinical treatment using functional materials for repairing osteoporotic bone defects.

**Keywords:** Osteoporotic fractures; Magnesium alloys; 3D printing; Bone defects repair; Surface modification

## 1. Introduction

Considering population aging, osteoporosis has become a global public health problem that cannot be ignored. Osteoporosis is characterized by decreased bone mass, increased bone fragility, and decreased bone strength caused by bone microstructure destruction. Osteoporotic bones are prone to fracture. According to statistics, more than 8.9 million osteoporotic fracture cases occur every year worldwide, with an average of one case of osteoporotic fracture every 3 s<sup>[1]</sup>. About 50% women and 20% men will have at least one osteoporotic fracture after the age of 50<sup>[2]</sup>. As the fracture site is extremely loose and the fracture is mostly comminuted, bone defects often form after fracture reduction. Neglecting treatment of bone defects may lead to delayed union, malunion, or nonunion of the fracture, which can seriously affect the quality of life of patients and even endanger their lives. Therefore, it is important to promote the repair of bone defects caused by osteoporotic fractures.

Autogenous bone graft, which is the traditional “gold standard” for filling bone defects, is not recommended for use in elderly patients considering several issues such as increased number of surgical sites, donor site infection, pain, and limited number of bone harvested<sup>[3]</sup>. Medical metal materials such as stainless steel (316SS), titanium (Ti) and its alloys, and cobalt-chromium (Co-Cr) alloys may cause many problems after implantation into the human body, such as stress shielding, toxic ion release, secondary surgery, and imaging artifacts<sup>[4]</sup>. Additionally, the repair of osteoporotic bone defects differs from that of common bone defects. The repair of defective parts is slow or impossible because of the imbalance between bone absorption and bone formation. This is mainly because osteoclast-mediated bone resorption is more pronounced than osteoblast-mediated bone formation in patients with osteoporosis, resulting in a reduced repair capacity<sup>[5]</sup>. Therefore, one of the major difficulties in promoting the repair of osteoporotic bone defects is to restore the balance between local osteogenesis and bone destruction.

As a new biodegradable metal material, magnesium (Mg) and its alloys have attracted much attention in the field of biomedical materials due to their excellent mechanical properties and good biocompatibility and biodegradability<sup>[6,7]</sup>. Most importantly, Mg implants can promote bone formation, increase mineral attachment and bone mass around the implants in the bone, and promote the repair of bone defects<sup>[8]</sup>. In addition, ideal bone implants should have interconnected porous structures similar to those of natural bone to facilitate the growth of new bone tissues and blood vessels<sup>[9]</sup>. For manufacturing porous Mg

alloy implants, traditional manufacturing methods (such as melt foaming, powder metallurgy, investment casting, etc.) cannot achieve precise control of the internal pore structure of porous Mg alloys, and it is impossible to prepare a fully interconnected complex porous structure<sup>[10]</sup>. In recent years, the development of three-dimensional (3D) printing technologies has made it possible to prepare Mg alloy bone-repair scaffolds with personalized interconnected porous structures and geometric shapes<sup>[11,12]</sup>. Previously, Mg alloy scaffolds have been successfully fabricated with a controllable appearance, good mechanical properties, and an interconnected porous structure through selective laser melting (SLM) technology; however, their very rapid degradation rate is not favorable for applications in clinical settings<sup>[13]</sup>.

Polysilazane is a polymer with Si-N as the main chain and can be converted into SiCN, SiCNO, or SiO<sub>2</sub> ceramics with excellent corrosion resistance under high-temperature conditions. Owing to the polarity of Si-N in its structure, the generated ceramics exhibited strong adhesion and could not easily fall off. Therefore, polysilazane is a good corrosion-resistant coating material and has broad application prospects in the construction of functional corrosion-resistant coatings, which is often used for metal anti-corrosion, carbon material anti-oxidation, organic material wear resistance, and other industrial fields, but it is rarely applied in the medical field<sup>[14]</sup>. Anti-osteoporosis drugs include anti-bone resorption and bone formation-promoting drugs. Bisphosphonates, a class of anti-bone resorption drugs, inhibit bone resorption by directly inhibiting the activation and proliferation of osteoclasts and are the most commonly used drugs in the treatment of osteoporosis<sup>[15,16]</sup>. As a third-generation bisphosphate preparation, zoledronic acid (ZA) has a high affinity for the surface of bone mineralization, especially for the active area of bone turnover, which mainly acts on osteoclasts, promotes osteoclast apoptosis, and inhibits bone resorption with a positive effect<sup>[17]</sup>. Local administration of bisphosphonates can expedite drug action and augment drug bioavailability<sup>[18]</sup>.

Here, we prepared biodegradable controllable 3D-printed Mg alloy scaffolds with a ZA-loaded ceramic corrosion control coating using 3D printing and surface modification technology. The degradation, biocompatibility, and bioactivity of the 3D-printed Mg alloy scaffolds were evaluated *in vitro* and *in vivo*. We expect to reduce the corrosion rate of Mg alloys by loading a ZA ceramic coating, which has the function of both Mg in promoting osteogenesis and ZA in inhibiting bone resorption, and introduce a method for promoting the healing of osteoporotic bone defects.

## 2. Materials and methods

### 2.1. Sample preparation and characterization

#### 2.1.1. Preparation of scaffolds and coating samples

The 3D-printed porous Mg alloy scaffolds were fabricated using a selective laser melting 3D printer as previously described<sup>[13]</sup>. The design porosity of 3D-printed Mg alloy scaffolds was 80%, and the design pore diameter was 600  $\mu\text{m}$ . The main component of the Mg alloy powder used for printing was Mg-3Nd-0.2Zn-0.4Zr, abbreviated as JDBM. The printed scaffolds were electrochemically polished. Square scaffolds with  $10 \times 10 \times 10$  mm diameters were fabricated for *in vitro* experiments, and cylindrical scaffolds with  $3 \times 4$  mm diameters were used for animal experiments. In addition,  $5 \times 5 \times 3$  mm cast Mg alloy bulk samples were prepared for coating characterization.

Further, 15 g butyl acetate and 5 g polysilazane were stirred under nitrogen for 1 h. Subsequently, 2 mg of ZA was added and stirred for 2 h to obtain polysilane coating materials containing ZA (332.6  $\mu\text{M}$ ). The JDBM Mg alloy samples were immersed into the coating material for 3 min. The ZA drug load of each sample was about 40  $\mu\text{g}$ . The prepared drug-loaded coating samples were heated in the oven at 150°C for 4 h; the ceramic-coated JDBM Mg alloy samples containing ZA are referred to as Mg/Sc/ZA hereafter. Pure ceramic coating samples without ZA were prepared using the same method and are referred to as Mg/Sc, and the uncoated JDBM Mg alloy samples are represented by Mg as the control group.

#### 2.1.2. Sample characterization

The surface morphology, cross-section, and elemental composition of the samples were examined using scanning electron microscopy (SEM, HITACHI S4800, Japan) combined with an energy dispersive X-ray spectrometer (EDS, OXFORD, UK). SEM images were analyzed and measured using the ImageJ 1.53e software (National Institutes of Health, USA) to obtain the pore diameter of scaffolds and the coating thickness of samples. The static contact angle (CA) and sliding angle (SA) of ultrapure water and hexadecane on the coating were measured using an optical contact angle tester (Attention Theta Flex, Switzerland). The coating adhesion of the samples was determined according to ASTM D3359-22.

#### 2.1.3. In vitro degradation

The 3D-printed Mg alloy scaffolds were immersed in simulated body fluid (SBF) for 7 days at 37°C. The pH, Mg ion concentration, and hydrogen release were measured every 24 h. After soaking for 7 days, the corrosion products were removed, and the surface morphology of the scaffolds was observed by SEM. The weight loss method is used

to calculate the degradation rate of the scaffolds, and the formula is as follows<sup>[13]</sup>:

$$\text{Degradation rate} = \frac{\text{Weight before soaking} - \text{Weight after soaking}}{\text{Soak time}} \quad (\text{I})$$

#### 2.1.4. Drug release in vitro

The 3D-printed Mg alloy scaffolds with ZA-loaded ceramic coating were placed in 15 mL of Dulbecco's phosphate-buffered saline (DPBS, pH = 7.4). Oscillate at a predetermined interval of 120 rpm in a constant temperature oscillator (ZD-85A, Langyue, China) at 37°C. Each time, 3 mL DPBS was taken out for analysis and replaced with the same amount of fresh DPBS. The concentration of ZA released into DPBS was measured using an ultraviolet-visible spectrophotometer (Evolution 201, Thermo Fisher Scientific, USA) at 210 nm wavelength.

### 2.2. In vitro cell experiments

#### 2.2.1. Preparation of scaffold extracts

According to ISO10993-12, the scaffolds sterilized with ethylene oxide were placed in Alpha-Modified Eagle Medium ( $\alpha$ -MEM, Hyclone, USA) containing 10% fetal bovine serum (FBS, Hyclone, USA) and 1% penicillin-streptomycin (Hyclone, USA) with a concentration of 0.1 g/mL. Subsequently, the culture medium was incubated in 37°C and 5%  $\text{CO}_2$  cell incubator for 72 h. The extracts were stored in refrigerator at 4°C for standby.

#### 2.2.2. Cell viability

Bilateral ovariectomy was performed in 3-month-old female Sprague-Dawley rats. Rat bone marrow mesenchymal stem cells (rBMSCs) were isolated and expanded 3 months after the operation, according to previously described methods<sup>[19]</sup>. The rBMSCs were seeded in 96-well plates at a density of  $2 \times 10^3$  cells/well. Twenty-four hours after inoculation, the original culture medium was replaced with scaffold extracts. The cells were incubated in 37°C, saturated humidity, and 5%  $\text{CO}_2$  for 1, 3, 5, and 7 days. Further, 100  $\mu\text{L}$   $\alpha$ -MEM and 10  $\mu\text{L}$  Cell Counting Kit-8 (Dojindo Molecular Technology, Japan) solution were added to each well and incubated at 37°C for 2 h. The optical density (OD) at 450 nm was measured using a microplate reader (Bio-Tek, USA) to determine cell viability.

#### 2.2.3. Osteogenic differentiation

The osteogenic differentiation of rBMSCs was evaluated using alkaline phosphatase (ALP) and Alizarin Red (AR) staining. The rBMSCs were seeded into 48-well plates at a density of  $1 \times 10^4$  cells/well. After the cells reached about 80% confluence, the medium was replaced with osteogenic differentiation medium (Sigma-Aldrich, USA) containing different scaffold extracts and supplemented with 10 mM

$\beta$ -glycerophosphate, 50 mM ascorbic acid, and 100 nM dexamethasone. As mentioned earlier<sup>[18]</sup>, ALP staining was performed on the day 7, and ALP activity was determined using an ALP detection kit (Beyotime Biotechnology, China) according to the manufacturer's instructions. To evaluate the formation of calcium nodules, rBMSCs were stained with Alizarin Red solution (Cyagen, USA) 21 days after osteogenic induction. After photography and recording, the mineralized nodules were dissolved in 10% cetylpyridine (Sigma-Aldrich, USA), and the absorbance at 562 nm was measured for semi-quantitative analysis.

#### **2.2.4. Tartrate-resistant acid phosphatase (TRAP) staining assay**

Mouse bone marrow-derived macrophages (BMMs) were isolated as previously described<sup>[20]</sup>. BMMs were seeded in 96-well culture plates at a density of  $8 \times 10^3$  cells/well and incubated different scaffold extracts containing 30 ng/mL macrophage colony-stimulating factor (M-CSF) and 100 ng/mL nuclear factor kappa B receptor activator ligand (RANKL; R&D, USA) for 5 days. On the 5th day, the cells were stained using a TRAP staining kit (Sigma-Aldrich, USA). After staining, the number and the area of TRAP-positive osteoclasts with three or more nuclei were counted and observed, respectively, with the aid of a light microscope (Leica, Germany) and analyzed using the ImageJ software.

#### **2.2.5. Actin ring formation assay**

BMMs were seeded in 48-well culture plates at a density of  $2 \times 10^4$  cells/well and treated with different scaffold extracts in the presence of M-CSF and RANKL for 5 days. The cells were stained with rhodamine-conjugated phalloidin (Abcam, UK) and subsequently stained with 4-amino-6-diamino-2-phenylindole (DAPI; Sigma-Aldrich, USA). Finally, the actin rings were observed and imaged using a fluorescence microscope (Leica, Germany).

#### **2.2.6. Bone resorption assay**

BMMs were seeded onto bovine bone slices in 96-well culture plates at a density of  $8 \times 10^3$  cells/well. The cells were treated with different scaffold extracts in the presence of M-CSF and RANKL. After 14 days, the cells on the bone slices were removed. Bone slices were coated with gold after gradient dehydration, and bone resorption was observed using SEM.

#### **2.2.7. Intracellular reactive oxygen species (ROS) assay**

BMMs were seeded on 35-mm petri dish at a density of  $3 \times 10^5$  cells/well and cultured in different scaffold extracts containing M-CSF and RANKL for 48 h. The cells were incubated at 10  $\mu$ M DCFH-DA (Beyotime Biotechnology, China) and observed under laser confocal scanning microscope (LCSM, Leica, Germany).

#### **2.2.8. Real-time quantitative polymerase chain reaction**

Real-time quantitative polymerase chain reaction (RT-qPCR) was performed as described previously<sup>[21]</sup>. Briefly, rBMSCs were seeded in 6-well culture plates at a density of  $2 \times 10^5$  cells/well and cultured with different scaffold extracts for 3 days. BMMs were seeded in 6-well culture plates at density of  $3 \times 10^5$  cells/well and cultured with different scaffold extracts containing M-CSF and RANKL for 3 days. Total RNA from rBMSCs and BMMs was separated using TRIzol reagent (Life Technologies, USA). According to the manufacturer's instructions, the total RNA was reverse-transcribed into complementary cDNA using PrimeScript RT kit (TaKaRa, Japan), and TB Green Premix Ex Taq (TaKaRa, Japan) was used for real-time PCR on QuantStudio 6 flex real-time PCR platform (Applied Biosystems, France). All the measured genes were normalized to *GAPDH* and calculated by the  $2^{-\Delta\Delta C_t}$  method. Primer sequences (Sangon Biotech Co., Ltd., China) are listed in Table 1.

### **2.3. In vivo animal experiments**

#### **2.3.1. Osteoporotic bone defects model**

Animal experiments were conducted in accordance with the relevant guidelines and approved by the Ethics Committee of the Ninth People's Hospital affiliated with the Shanghai Jiao Tong University School of Medicine. In this study, 60 three-month-old female Sprague-Dawley rats (Shanghai Sipper BK Laboratory Animals Ltd., Shanghai, China) were used for the *in vivo* experiments. A rat model of osteoporosis was established by ovariectomy to simulate postmenopausal osteoporosis as described previously<sup>[18]</sup>. A tube with a diameter of 3 mm was formed on the outside of the right femoral condyle using a drill bit, and 3D-printed Mg alloy implants were implanted into the tube. The animals were euthanized 3, 6, and 9 weeks after implantation to evaluate the effect of the implants on the repair of osteoporotic bone defects.

#### **2.3.2. X-ray and micro-computed tomography**

A Multifocus X-ray system (Faxitron, Biotics, USA) was used to examine the anteroposterior and lateral plain films of the right femur according to the manufacturer's instructions. After fixation in 4% paraformaldehyde, the femur specimens were scanned by micro-computed tomography (micro-CT; SCANCO Medical AG, Bassersdorf, Switzerland). The femoral condyle was considered as the region of interest (ROI). High-resolution 3D reconstruction of the femoral condyle was also performed. The residual volume of scaffolds, bone mineral density/bone volume (BMD/BV), bone volume/tissue volume (BV/TV), mean trabecular thickness (Tb.Th), and mean trabecular spacing (Tb.Sp) were quantitatively analyzed.



**Table 1.** Primer sequences for RT-qPCR

Gene	Forward primer sequence (5'-3')	Reverse primer sequence (5'-3')
<i>GAPDH1</i>	CTGGAGAAACCTGCCAAGTATG	GGTGGAAGAATGGGAGTTGCT
<i>Alpl</i>	CGGCACCTGCCTTACCAACT	ACTGTGGAGACGCCCATACC
<i>Spp1</i>	GATGAACAGTATCCCGATGCCA	GTCTTCCCGTTGCTGTCCTGA
<i>Runx2</i>	CAGTATGAGAGTAGGTGTCCCGC	AAGAGGGGTAAGACTGGTCATAGG
<i>Col1a1</i>	CGTGGAAACCTGATGTATGCTTG	CCTATGACTTCTGCGTCTGGTGA
<i>SP7</i>	CTGGGAAAAGGAGGCACAAAGA	GGGGAAAGGGTGGGTAGTCATT
<i>Bglap</i>	AGGGCAGTAAGGTGGTGAATAGA	GAAGCCAATGTGGTCCGCTA
<i>GAPDH2</i>	CCTCGTCCCGTAGACAAAATG	TGAGGTCAATGAAGGGGTCGT
<i>C-Fos</i>	CGAAGGAACGGAATAAGATG	TGGGAAGCCAAGGTCATCG
<i>Acp5</i>	CACGATGCCAGCGACAAGA	TGAAGCGCAAACGGTAGTAAGG
<i>CTSK</i>	GTTGACTTCCGCAATCCTTACC	CAGCAGAACTTGAACACCCAC
<i>Nfatc1</i>	CACTCCACCCACTTCTGACTTCC	GGCTGCCTTCCGTCTCATAGTG
<i>Calcr</i>	CAACCGAACCTGGTCCAACATAT	GACAAGGAGTGACCCACAAGAG
<i>MMP9</i>	GCTGGCAGAGGCATACTTGATAC	CAGTATGTGATGTTATGATGGTCCC

Note: *GAPDH1* represents glyceraldehyde-3-phosphate dehydrogenase gene of rat, and *GAPDH2* represents glyceraldehyde-3-phosphate dehydrogenase gene of mouse.

### 2.3.3. Histological evaluation

The femur specimens were fixed in 4% paraformaldehyde for 72 h and decalcified using ethylenediaminetetraacetic acid (EDTA). All decalcified femur specimens were embedded in paraffin for histological slicing after the 3D-printed Mg alloy implants were removed. The slices were stained with hematoxylin and eosin (HE), Masson's trichrome, and TRAP. In addition, OPN and RUNX2 immunohistochemical staining were performed.

### 2.3.4. Biocompatibility evaluation in vivo

Nine weeks after Mg alloy scaffold implantation, blood samples from animals in each group were collected before euthanasia, and the serum Mg concentration and liver and kidney function indices were tested. After euthanasia, the liver, kidney, heart, spleen, and lung were taken out of each animal from every group immediately. The morphologies of the visceral tissue were evaluated after paraffin embedding, slicing, and HE staining.

### 2.4. Statistical analysis

The data were expressed as mean  $\pm$  standard deviation (SD) of at least three independent experiments. The results were analyzed by the Student's *t* test or one-way analysis of variance (ANOVA) using SPSS29.0 software (IBM Corp., USA). Statistical significance was set at  $P < 0.05$ .

## 3. Results

### 3.1. Coating samples characterization

As shown in Figure 1A, thicknesses of the coatings on the bulk samples of the Mg/Sc and Mg/Sc/ZA groups were

uniform. EDS showed that the surface coating of Mg/Sc group was mainly composed of C, N, Si, and O elements, which are ceramic material formed by polysilazane at high temperature. Further, N and P appeared in the coating of the Mg/Sc/ZA group, indicating that the coating contained ZA. The two groups of coating elements were evenly distributed (Figure 1B). Figure 1C shows the general morphology of the 3D-printed Mg alloy scaffolds before and after coating; the length, width, and height of the scaffolds were all 10 mm. The surface morphology of the scaffolds before and after coating was observed by SEM, as shown in Figure 1D. The pore size distribution of the scaffolds before and after coating was uniform, and the surface of the uncoated scaffolds was smooth after polishing, while the surface of the coated scaffolds (Mg/Sc group and Mg/Sc/ZA group) was rough owing to the deposition of polysilazane. In addition, the measurement results showed no significant differences in the pore size of the Mg alloy scaffolds among the three groups, indicating that the coating had little effect on the pore characteristics of the porous scaffolds. There was no significant difference in coating thickness between the Mg/Sc and Mg/Sc/ZA groups (Figure 1E).

The effects of the coating on the hydrophobic and oleophobic properties of the Mg alloy samples are shown in Figure 1F. The water contact angle (WCA) of the Mg alloy sample increases significantly, and the water sliding angle (WSA) decreases significantly after coating, proving that the ceramic coating can weaken the surface hydrophilicity of the Mg alloy samples and enhance their hydrophobicity. The right side of Figure 1F shows a similar trend. The

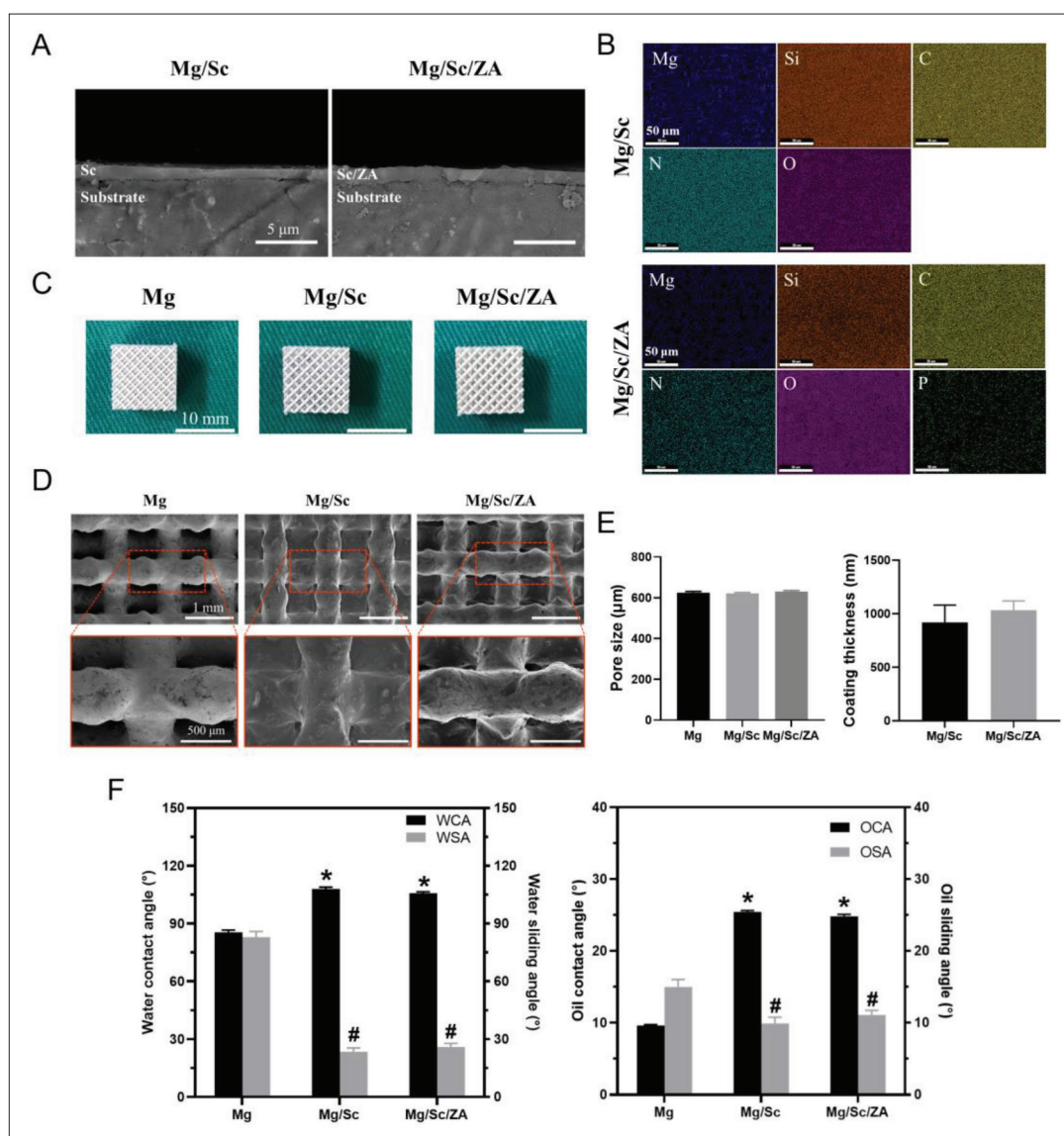


**Figure 1.** Characterization of magnesium (Mg) alloy coating samples. (A) The cross-sectional image of the coating using SEM. (B) EDS plane-scan results of Mg alloy bulk samples. (C) Pictures of Mg alloy scaffolds. (D) SEM surface micrographs of Mg alloy scaffolds. (E) Pore size (left) and coating thickness (right) of Mg alloy samples. (F) Contact angle and sliding angle of Mg alloy samples to water (left) and hexadecane (right) before and after being coated with polysilazane. \* $P < 0.05$  and # $P < 0.05$  vs. Mg group.

interfacial adhesion between the ceramic coating and Mg alloy sample and the hardness of the coating are listed in Table 2. The pencil hardness of the Mg alloy sample increased after coating. The coating was closely bonded to the Mg alloy substrate, particularly in the Mg/Sc group. The adhesion grade of the coating in the Mg/Sc group was 5B, and that of the Mg/Sc/ZA group was 4B, which meets the application requirements of most clinical scenarios. The adhesion of the Mg/Sc/ZA group was lower than that of the Mg/Sc group, possibly because, after loading ZA, the drug particles in the coating affected the uniformity and integrity of the ceramic coating.

**Table 2.** Pencil hardness and adhesion of ceramic coating

	Pencil hardness	Adhesion
Mg	3H	–
Mg/Sc	4H	5B
Mg/Sc/ZA	4H	4B

### 3.2. In vitro degradation and drug release

The SEM images of the surface morphologies of samples after the removal of degradation products are shown in Figure 2A. The corrosion of scaffolds in the Mg group was the most obvious. The structure of the scaffolds was

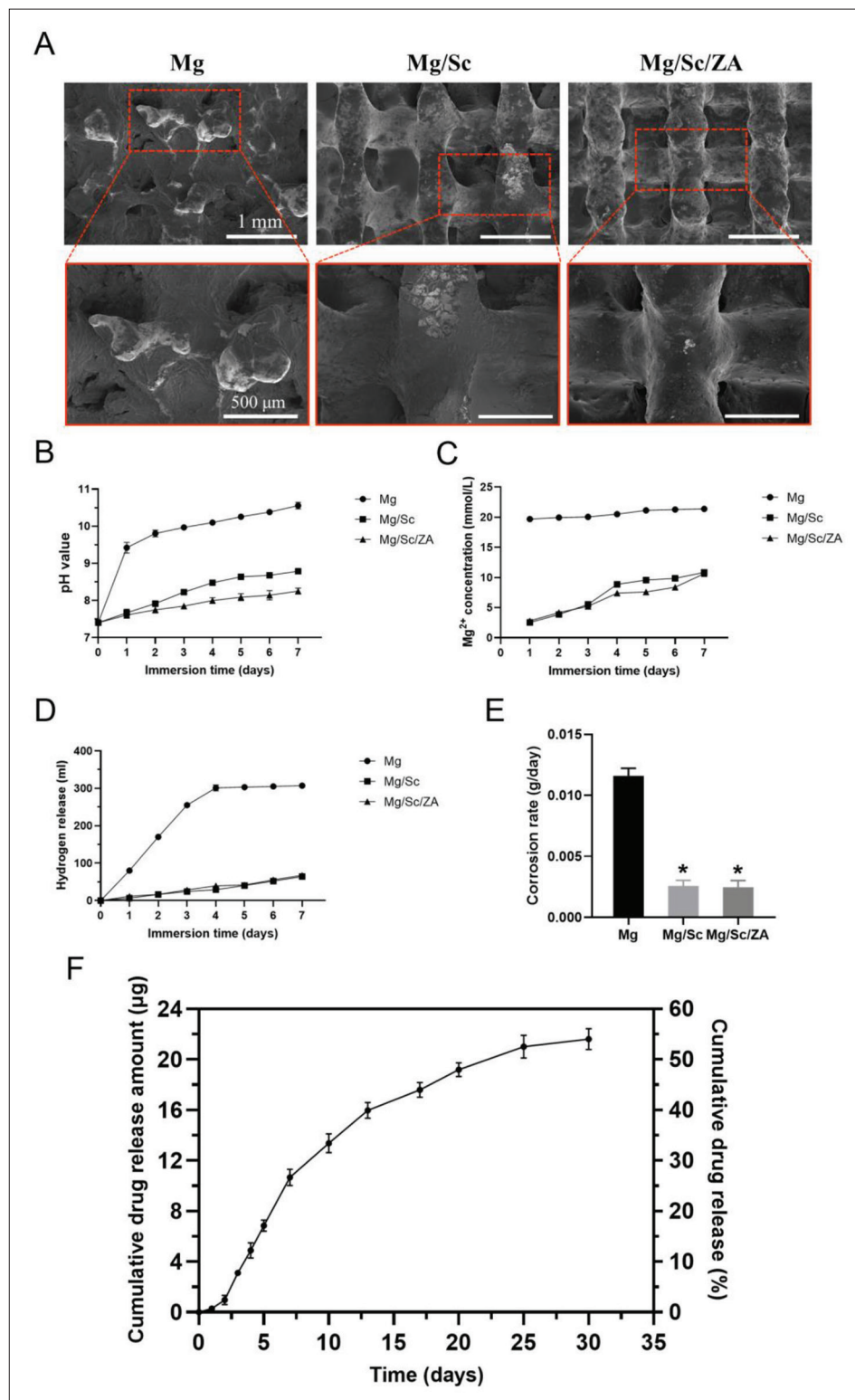


**Figure 2.** Degradation behavior and drug release of 3D-printed magnesium (Mg) alloy scaffolds *in vitro*. (A) Surface morphology of Mg alloy scaffolds after immersion for 7 days. The pH value (B),  $Mg^{2+}$  concentration (C), hydrogen release (D), and corrosion rate (E) of Mg alloy scaffolds within 7 days of immersion. (F) Zoledronic acid release curve of 3D-printed Mg alloy scaffolds loaded with zoledronic acid *in vitro*. \* $P < 0.05$  vs. Mg group.

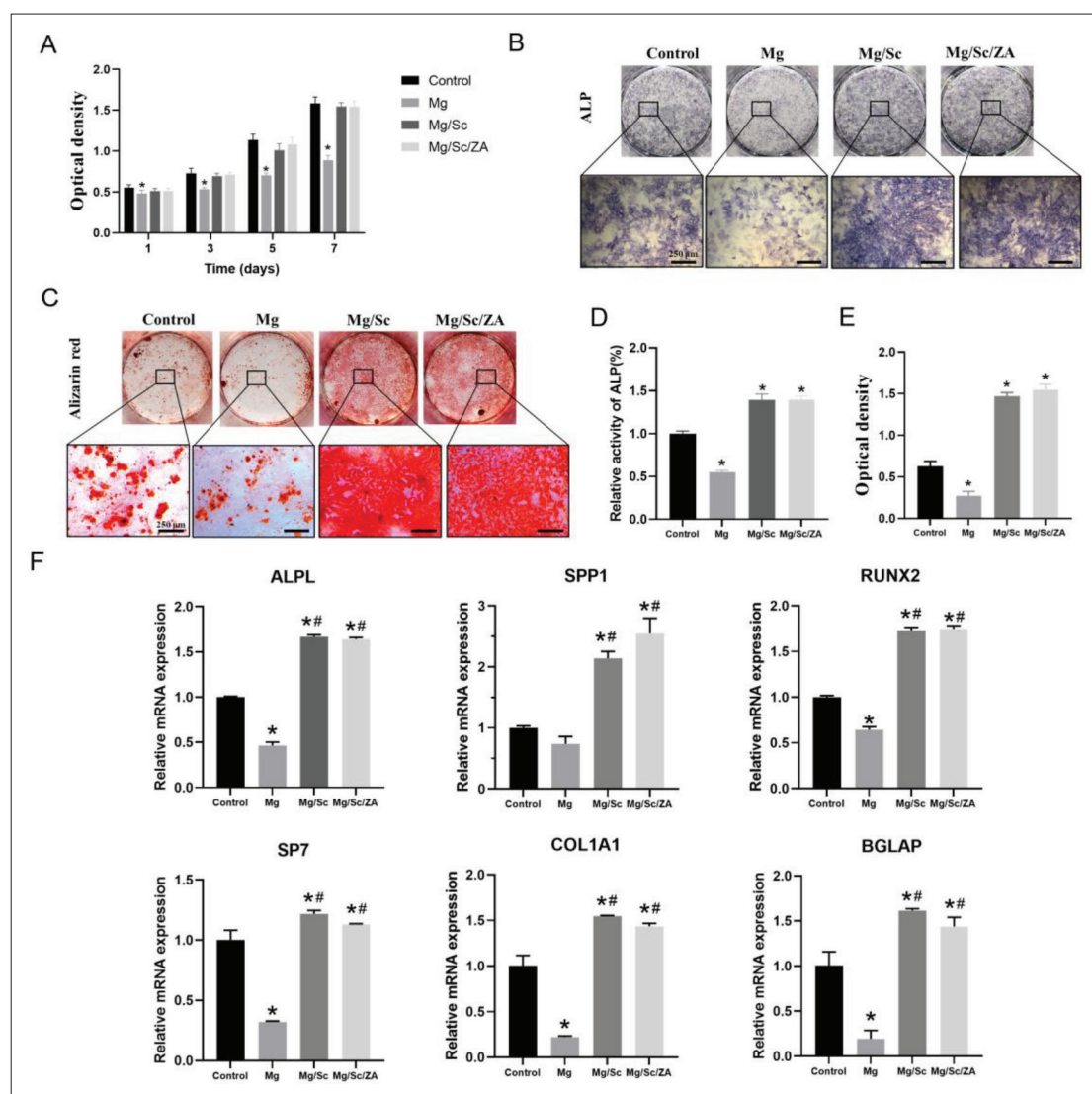


**Figure 3.** Cytocompatibility and osteogenic differentiation of rBMSCs cultured in the extract of naked JDBM (Mg), Mg/Sc, and Mg/Sc/Zn samples, respectively. (A) Cell viability. (B) ALP staining after 7 days of culture. (C) Alizarin red staining at 21 days. (D) Statistical analysis of relative activity of ALP at 7 days. (E) Semi-quantitative analysis of alizarin red staining for 21 days. (F) Relative expression of osteogenic differentiation related genes. \* $P < 0.05$  vs. Control group; # $P < 0.05$  vs. Mg group.

severely damaged, and there were many degradation products on the surface of the scaffolds. Corrosion of the scaffolds was the least in the Mg/Sc/Zn group, and there was almost no corrosion cracking on the scaffolds. During the entire *in vitro* degradation process, the pH,  $Mg^{2+}$  concentration, and hydrogen release of the Mg group were significantly higher than those of the Mg/Sc and Mg/Sc/Zn groups (Figure 2B–D). Additionally, the degradation rates of the Mg/Sc and Mg/Sc/Zn groups were significantly lower than those of the uncoated Mg alloy scaffolds in the Mg group (Figure 2E).

The *in vitro* drug release results are shown in Figure 2F. The release of ZA from the scaffold coating *in vitro* was

slow and controllable, and the release rate was slow at first, then fast, and finally decreased until it gradually stabilized. The release rate of ZA was similar to that of the scaffolds, indicating that the release of ZA was mainly controlled by degradation of the drug-loaded coating. The proportion of ZA released in the first 3 days was approximately 8%, and the cumulative release rate of ZA was 54% after soaking for 30 days.

### 3.3. *In vitro* cytocompatibility

The effect of the 3D-printed Mg alloy scaffold extracts from different groups on the proliferation of BMSCs from osteoporotic rats *in vitro* is shown in Figure 3A. Cell proliferation in the Mg/Sc and Mg/Sc/Zn groups was



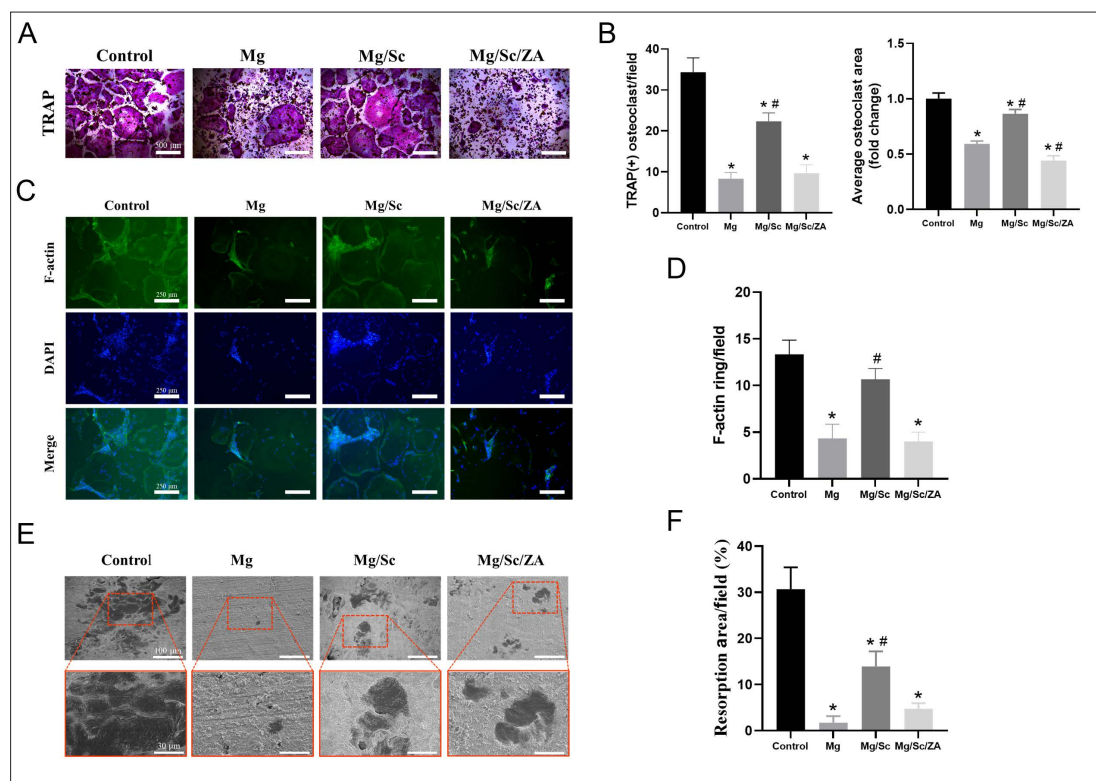


**Figure 4.** Osteoclast formation and bone resorption of BMMs cultured in the extract of magnesium (Mg) alloy scaffolds and stimulated with RANKL (100 ng/mL). (A) Representative images of TRAP-positive osteoclasts. (B) Quantification of the number (left) and the average area (right) of TRAP-positive multinucleated osteoclasts. (C) Representative images of F-actin ring formation in osteoclasts. (D) Quantification of the average number of F-actin ring; (E) Representative SEM images of bone resorption. (F) Quantification of resorbed bone slice area. \* $P < 0.05$  vs. Control group; # $P < 0.05$  vs. Mg group.

slightly lower than that in the control group; however, the difference was not statistically significant. On the 1st 3rd, 5th, and 7th days, the OD value of the Mg group was significantly lower than that of the control group, indicating that the alkaline environment and excessive concentration of Mg ions after the rapid degradation of the Mg alloy slowed down the proliferation rate of rBMSCs. Under the protection of the ceramic coating converted by polysilazane, the degradation rate of the Mg alloy substrate of the Mg/Sc and Mg/Sc/ZA groups decreased, and the physical and chemical properties of the culture medium minimally changed; therefore, the cell proliferation of the Mg/Sc and Mg/Sc/ZA groups was not significantly affected.

### 3.4. Osteogenic differentiation

The effect of the 3D-printed Mg alloy scaffold extracts on the osteogenic differentiation ability of rBMSCs is shown in Figure 3. Figure 3B and C shows that the degree of ALP and Alizarin Red staining in the Mg group was significantly weaker than that in the control group, whereas those in the Mg/Sc and Mg/Sc/ZA groups were significantly stronger than those in the control group. The relative activity of ALP in the Mg group was significantly lower than that in the control group, whereas that in the Mg/Sc and Mg/Sc/

ZA groups was significantly higher than that in the control group (Figure 3D), indicating that the environment of rapid degradation of the Mg alloy in the Mg group was not conducive to osteogenic differentiation of rBMSCs. In contrast, the degradation products produced in the Mg/Sc and Mg/Sc/ZA groups were beneficial for osteogenic differentiation of rBMSCs because of the slow degradation of the Mg alloy. In addition, there was no significant difference between the Mg/Sc and Mg/Sc/ZA groups. Therefore, the addition of ZA had no significant effect on early osteogenic differentiation of rBMSCs. The semi-quantitative results for the mineralized nodules were similar to those for ALP activity (Figure 3E). As shown in Figure 3F, the expression of ALPL, SPP1, RUNX2, SP7, COL1A1, and BGLAP related to bone differentiation in the Mg/Sc and Mg/Sc/ZA groups was significantly higher than that in the control and Mg groups, further confirming that the Mg/Sc/ZA extracts can promote osteogenic differentiation *in vitro*.

### 3.5. Osteoclastogenesis, bone resorption, and intracellular reactive oxygen species

TRAP staining results are shown in Figure 4A. Quantitative statistics showed that the area and number

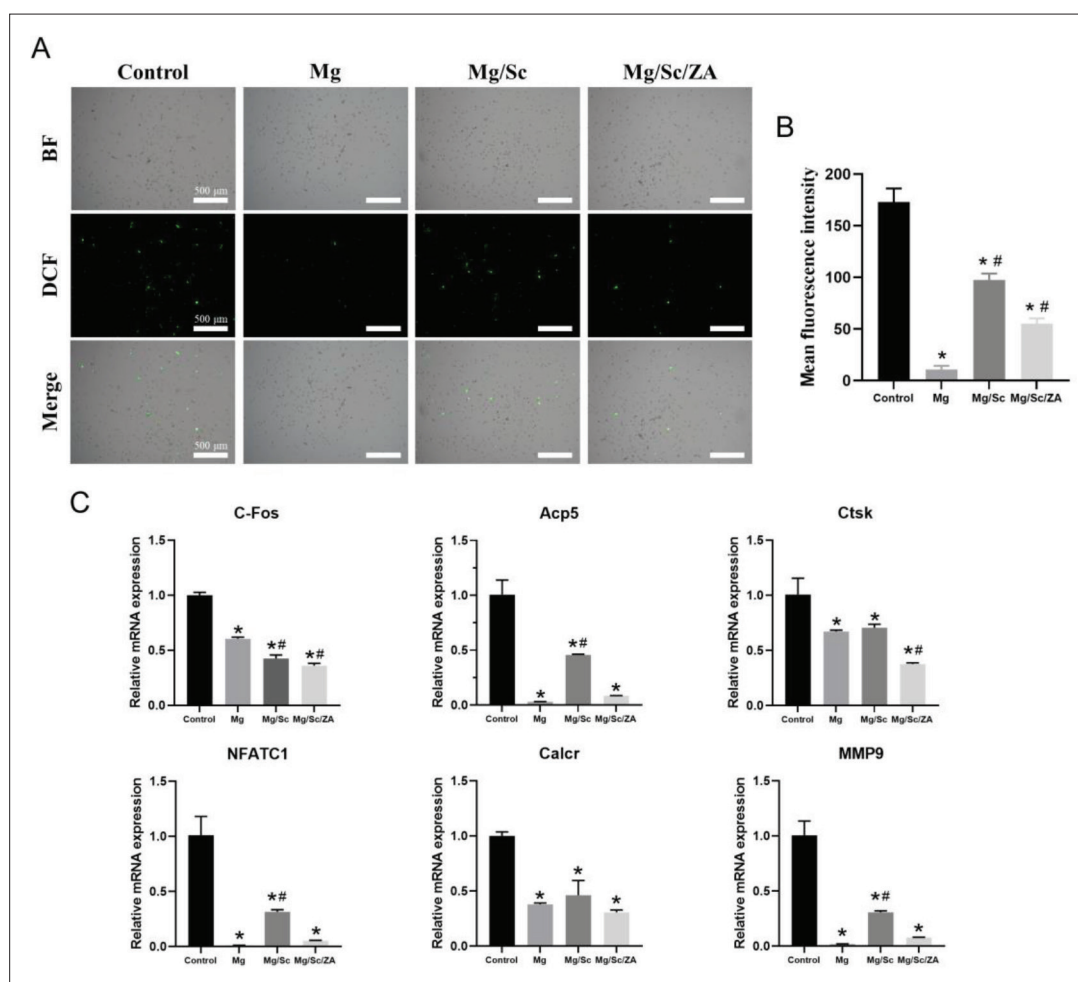


**Figure 5.** Reactive oxygen species (ROS) levels and the expression of osteoclast differentiation genes in BMMs cultured in the extract of naked JDBM (Mg), Mg/Sc, and Mg/Sc/ZA samples and stimulated with RANKL (100 ng/mL) for 5 days. (A) Representative images of ROS in BMMs cells under fluorescence microscope for 48 h. (B) Quantitative ROS fluorescence intensity. (C) Relative expression of osteoclast-specific genes. \* $P < 0.05$  vs. Control group; # $P < 0.05$  vs. Mg group.

of TRAP-positive osteoclasts in the control group were significantly higher than those in the other three groups. The number and area of TRAP-positive osteoclasts in the Mg group were lowest, whereas those in the Mg/Sc group were relatively large (Figure 4B). The reason for the small number and area of osteoclasts in the Mg group was that the environment formed by the rapid degradation of the Mg alloy in the Mg group was disadvantageous for the growth and differentiation of osteoclasts. A comparison of staining results between the Mg/Sc and Mg/Sc/ZA groups showed that ZA released by the Mg alloy coating in the Mg/Sc/ZA group effectively inhibited osteoclast differentiation and hindered osteoclast formation and further differentiation. The inhibitory effect of the Mg/Sc/ZA scaffold extracts on osteoclast differentiation was confirmed by staining osteoclast actin rings with rhodamine-conjugated phalloidin (Figure 4C). Quantitative analysis revealed that

the average number of F-actin rings in the Mg and Mg/Sc/ZA groups was significantly lower than that in the control group (Figure 4D). As shown in Figure 4E, the bone resorption area of Mg group is negligible and the area of bone resorption area is the smallest. Quantitative analysis of the resorption area showed that the bone resorption area in the Mg, Mg/Sc, and Mg/Sc/ZA groups was significantly lower than that in the control group, and there was a significant difference between the Mg and Mg/Sc groups (Figure 4F). It can be concluded that extracts of the coating samples of the Mg/Sc/ZA group significantly inhibited osteoclast bone resorption through the slow release of ZA. In addition, the expression levels of osteoclast differentiation-related genes, such as *c-Fos*, *Acp5*, *Ctsk*, *NFATc1*, *Calcr*, and *MMP9*, were significantly lower than those in the control group (Figure 5C). From the results of the detection and quantitative analysis, it was found that

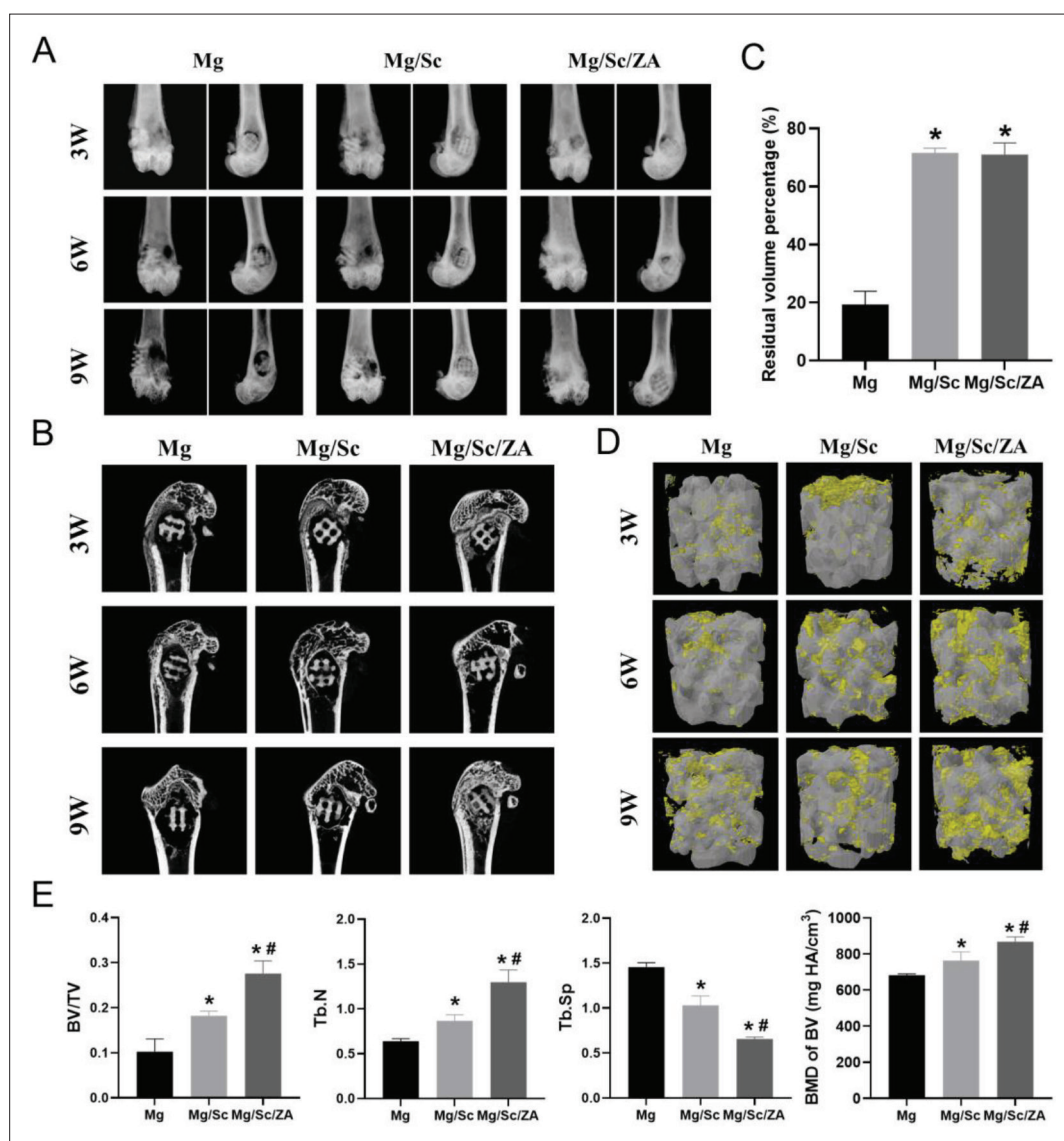


**Figure 6.** Radiological evaluation of osteoporotic bone defect healing. (A) Anterior and lateral X-ray images of distal femur of osteoporotic rats. (B) Micro-CT of femoral samples of osteoporotic rats. (C) Quantification of residual volume percentage. (D) Three-dimensional reconstruction of implant. (E) Quantification of the parameters included BV/TV, Tb.N, Tb.Sp, and BMD of BV. 3W, 6W, and 9W in (A), (B), and (D) represent 3 weeks, 6 weeks, and 9 weeks, respectively. \* $P < 0.05$  vs. Mg group; # $P < 0.05$  vs. Mg/Sc group.

the fluorescence intensity of reactive oxygen species (ROS) in the Mg/Sc/ZnA group was significantly lower than that in the control and Mg/Sc groups. Cell survival was lower in the Mg group, and the fluorescence intensity of ROS was the lowest in the Mg group (Figure 5A and B).

### 3.6. Effect of 3D-printed Mg alloy scaffolds on osteoporotic bone defect repair

#### 3.6.1. Radiographic analysis

The anteroposterior and lateral X-ray films of femur at different time points in each group are shown in Figure 6A. The defect healing rate in the Mg/Sc/ZnA group was

significantly higher than those in the Mg and Mg/Sc groups. The degradation rate of the 3D-printed Mg alloy scaffolds in the Mg/Sc and Mg/Sc/ZnA groups was also significantly lower than that in the Mg group. The degradation of the Mg alloy scaffolds was similar to that induced by X-rays. Quantitative analysis of the residual volume of the scaffolds confirmed this observation (Figure 6C). Micro-CT scans and reconstructed images of each group at different time points are shown in Figure 6B and D. The results showed that new bone tissue appeared around the 3D-printed Mg alloy porous scaffolds in the Mg/Sc/ZnA group 3 weeks after implantation, and a large amount of new bone tissue grew



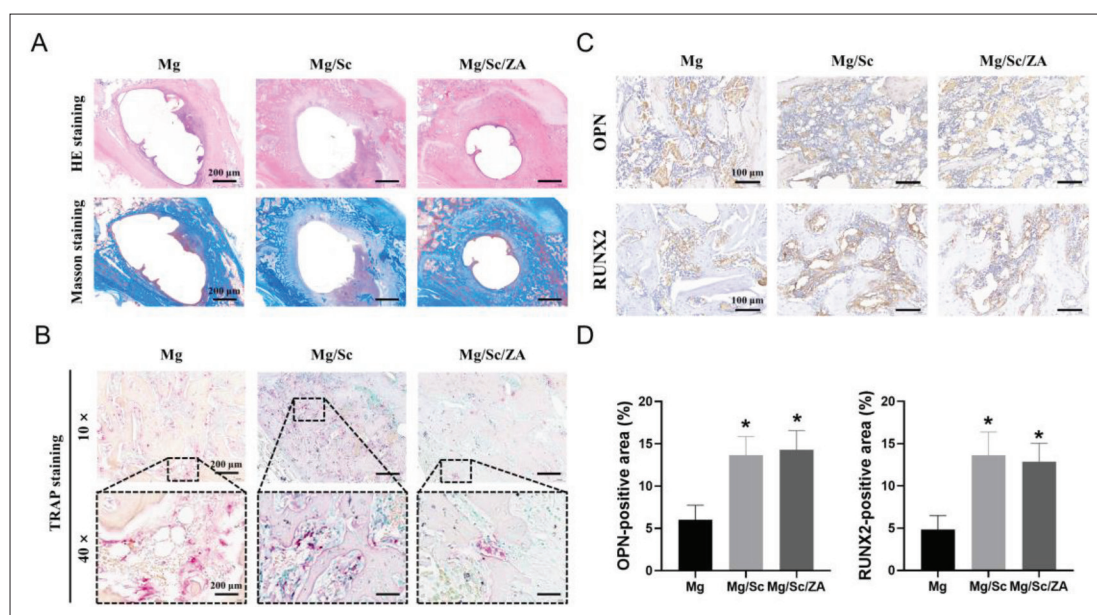


**Figure 7.** Histological evaluation of osteoporotic bone defect healing 9 weeks after implantation. (A) Representative images of HE and Masson's trichrome staining of femoral tissue sections. (B) Representative images of TRAP staining of femoral tissue sections. (C) Representative images of immunohistochemistry staining. (D) Quantification of the proportion of immunohistochemical staining-positive areas. \* $P < 0.05$  vs. Mg group.

into the scaffold 9 weeks after implantation. There was only a small amount of new bone around the scaffolds in the Mg/Sc group, and less around the scaffold in the Mg group. Quantitative analysis of the related measurement indices of micro-CT (Figure 6E) showed that 9 weeks after the operation, the number of trabeculae in the Mg/Sc/ZA group was the highest, while the trabecular separation degree was the lowest. Compared with uncoated scaffolds in Mg group, the BMD and BV/TV of femur specimens in Mg/Sc group and Mg/Sc/ZA group were significantly higher, and the difference was statistically significant.

### 3.6.2. Histological evaluation

HE and Masson's trichrome staining showed that the healing of bone defects in the Mg/Sc/ZA group was better than that in the Mg and Mg/Sc groups, and trabecular growth was observed at the edge of the defect; however, there was no obvious bone growth in the Mg and Mg/Sc groups (Figure 7A). TRAP staining *in vivo* revealed that the red staining area in the Mg/Sc/ZA group was smaller than that in the Mg and Mg/Sc groups at low magnification (Figure 7B). However, a large number of osteoclasts were observed in the Mg and Mg/Sc groups under a high-power microscope, which was consistent with the results of TRAP staining *in vitro*. The results showed that ZA released by the drug-loaded coating effectively inhibited osteoclast formation in osteoporotic rats. As shown in Figure 7C and D, the areas positive for OPN and RUNX2 in the Mg/Sc and Mg/Sc/ZA groups were significantly larger than those in the Mg group. The rapid degradation of uncoated

Mg alloy scaffolds releases excess Mg ions and forms an alkaline microenvironment that is not conducive to the expression of osteogenic differentiation proteins. The Mg ions released by the slow degradation of the Mg alloy in the coating group promoted the expression of OPN and RUNX2, which are the osteogenic differentiation proteins.

### 3.6.3. In vivo biocompatibility

As shown in Figure 8A, the morphology of the cells in the heart, liver, spleen, lung, and kidney in the Mg, Mg/Sc, and Mg/Sc/ZA groups was normal, and no abnormal histological changes were observed compared with the control group. In addition, there were no significant differences in the serum Mg concentration and other biochemical indices between the scaffold implantation and control groups (Figure 8B). The results showed that the 3D-printed porous Mg alloy scaffold coated with polysilazane exhibited high biological safety and good biocompatibility *in vivo*.

## 4. Discussion

Compared to the degradable polymers and bioceramics commonly used in Mg alloy coatings, ceramic coatings cured by polysilane were more closely combined with the Mg alloy substrate, and the ceramic coating had higher hardness and excellent hydrophobic properties, which could significantly delay the degradation process of the scaffolds. The degradation experiments *in vitro* showed that the polysilane ceramic coating can reduce the average



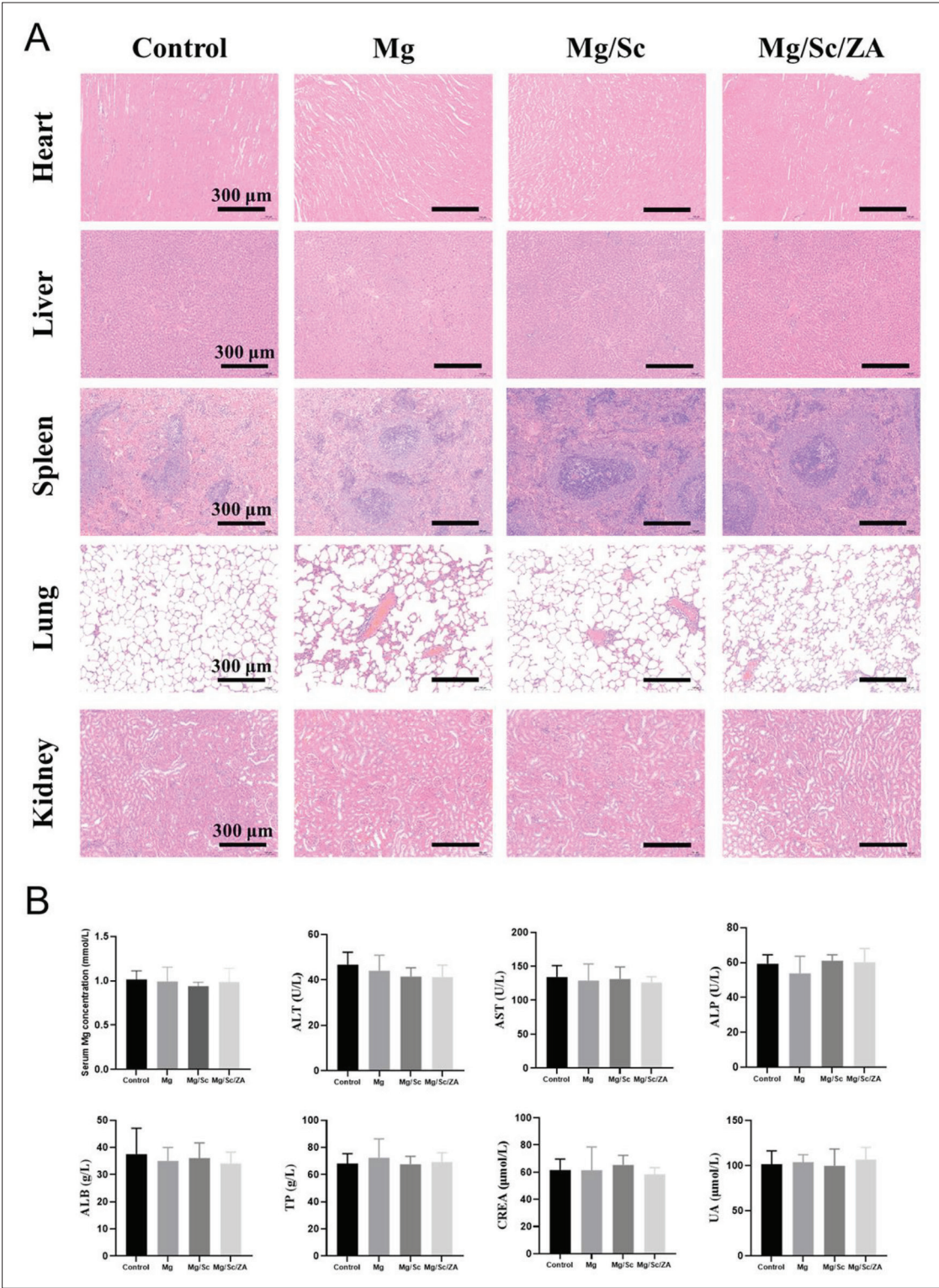


**Figure 8.** Biosafety evaluation of 3D-printed magnesium (Mg) alloy scaffolds *in vivo*. (A) Representative histological images of HE staining of main visceral tissue sections of osteoporosis rats. (B) Serum Mg ion concentration and biochemical indexes of osteoporotic rats.

degradation rate of 3D-printed Mg alloy scaffolds *in vitro* from  $11.60 \pm 0.05$  mg/day to  $2.47 \pm 0.45$  mg/day, which is only about 21% of the original rate, greatly improving the corrosion resistance of 3D-printed Mg alloy scaffolds. The calcium phosphate material commonly used for Mg alloy surface coatings could only reduce the degradation rate of JDBM Mg alloy bars to 72% of the original rate<sup>[22]</sup>, and the protective effect of the coating on the Mg alloy substrate was significantly weaker than that of a polysilane ceramic coating.

We found that when the Mg-based implant degraded too quickly, a high concentration of Mg ion simultaneously inhibited the proliferation and differentiation of osteoblasts and osteoclasts. These results are consistent with those of previous studies showing that alkaline microenvironments with high Mg ion concentration as a result of Mg degradation can inhibit new bone regeneration and absorption<sup>[23,24]</sup>. Therefore, it is necessary to adjust the degradation rate of Mg alloys to release an appropriate amount of Mg ions to promote osteogenesis. Some studies have shown that a Mg ion concentration of approximately 2 mM promotes the proliferation and differentiation of osteoblasts *in vitro* and formation of new bones *in vivo*<sup>[25]</sup>. The effect of osteogenic induction is best when the concentration of Mg ions is in the range of 2.5 to 5 mM<sup>[26]</sup>. However, when the concentration of Mg ions is more than 10 mM, it will begin to inhibit the osteogenic differentiation. When the concentration of Mg ion exceeds 20 mM, it will even lead to a significant increase in cell apoptosis. The *in vitro* degradation experiment showed that the concentration of Mg ions produced by the 3D-printed Mg alloy scaffolds in the ceramic coating group in the early stage of degradation was approximately 2.5 mM, and then slowly increased to 10 mM. After implantation, because of absorption in the peripheral blood circulation, the concentration of Mg ions in the implantation area is often lower than the *in vitro* degradation concentration in the same period<sup>[27]</sup>. Therefore, it can be speculated that ceramic-coated Mg alloy scaffolds implanted into the body form a microenvironment in which the concentration of Mg ions is less than 10 mM, which is conducive to osteogenic differentiation. The released Mg ions can upregulate expression of osteogenic-related genes, promote the proliferation and differentiation of osteoblasts, and accelerate the growth of new bone in the bone defect. The future research goal is to achieve a precise match between the scaffold degradation rate and the bone growth rate by adjusting the coating thickness, which will lead to complete repair of the defect when the scaffold is completely degraded.

The number of BMSCs involved in bone repair and their differentiated osteoblasts in patients with osteoporotic bone defects decreased, and their function was low, while the osteoclasts were abnormally active, resulting in slow rate and prolonged time of defect repair<sup>[28]</sup>. Based on this,

we loaded ZA into the ceramic composite coating on the surface of 3D-printed Mg alloy scaffolds and promoted the healing of osteoporotic bone defects through the joint action of Mg ions released from the degradation of Mg alloy scaffolds and ZA loaded on the coating. In view of the obvious adverse effects of ZA in systemic application and the small effect of the drug on local lesions<sup>[29,30]</sup>, we adopted the method of combining scaffold implantation with local drug delivery. ZA was added to the coating material to coat the surface of the scaffolds, and the drug was released slowly and controllably with the degradation of the scaffolds to achieve local controlled release and slow release of the drug. *In vitro* drug release experiments showed that ZA was released stably from the scaffold surface at a relatively low rate, and the release rate reached 54% within 30 days, indicating the sustained release of the drug. When the Mg alloy scaffolds were degraded, ZA loaded on the coating was released slowly and acted directly on the defect area with Mg ions at the same time. The results showed that ZA released from the coating during degradation did not affect the effect of Mg ions on osteogenesis, but it significantly inhibited active osteoclast differentiation and bone resorption in rats with osteoporosis by inhibiting osteoclast formation, downregulating the expression levels of osteoclast-related genes and subsequently increasing bone density and bone strength. The results of this study suggest that combining the osteogenic effect of Mg with the inhibitory effect of ZA on osteoclasts can improve the dynamic balance between bone formation and resorption in the local environment and promote repair and reconstruction of osteoporotic bone defects.

In addition, the effect of hydrogen produced by the degradation of Mg alloys must be considered. Hydrogen is an important degradation product of Mg. When the degradation rate of Mg alloy implants *in vivo* is too rapid, the hydrogen produced cannot be absorbed by the body in time and accumulates in the implanted area to form a subcutaneous cavity. The rapid accumulation of hydrogen delays bone healing, forms obvious tissue calluses, blocks blood flow, and leads to tissue necrosis<sup>[31]</sup>. Therefore, it is necessary to adjust the degradation rate of Mg alloys to reduce hydrogen production. Although a large amount of hydrogen has adverse effects on patients, hydrogen, as an important pathophysiological regulator, has great potential to regulate oxidative stress, inflammation, and apoptosis<sup>[32]</sup>. Hydrogen not only reduces oxidative stress by directly reacting with strong oxidants, but also indirectly reduces oxidative stress by regulating the expression of various genes<sup>[33]</sup>. In this study, the detection of ROS in osteoclasts showed that the average fluorescence intensity of ROS in the Mg alloy group was significantly lower than that in the control group, demonstrating that the

degradation products of the Mg alloy scavenged ROS and reduced oxidative stress. Future research should focus on the effect of hydrogen released by Mg alloy degradation on osteoblast and osteoclast differentiation, the control of hydrogen production rate, and the rational use of the hydrogen environment to accelerate bone defect repair.

This study had some limitations. First, the specific molecular mechanism by which Mg ions and ZA regulate the osteoblast and osteoclast balance has not been clearly explored. Second, further exploration in the adjustment of the degradation rate of 3D-printed biodegradable Mg alloy scaffolds with a ZA-loaded ceramic composite coating, so that the scaffold degradation rate can accurately match the new bone growth rate, is needed.

## 5. Conclusion

The present study focused on the investigation of 3D-printed biodegradable Mg alloy materials in a bid to address the clinical problem of osteoporotic bone defects. The osteogenic effect of Mg ions and ZA on the inhibition of osteoclasts was coupled by means of a drug-loaded coating on the surface of Mg-based implants to adjust the balance of bone formation/resorption and promote the repair of osteoporotic bone defects. We prepared a ceramic coating loaded with ZA on the surface of 3D-printed Mg alloy porous scaffolds, which exhibited excellent hydrophobic and oleophobic properties and excellent adhesion. The coating not only significantly reduces the degradation rate of the Mg alloy substrate *in vitro* but also provides controlled and slow release of loaded drugs. The drug-loaded ceramic-coated 3D-printed Mg alloy scaffolds have the biological function of regulating osteoblast/osteoclast differentiation. Animal experiments confirmed that the ceramic coating on the surface of the 3D-printed Mg alloy scaffolds effectively delayed the degradation rate in ovariectomized rats, and bone ingrowth and bone defect healing were better in the drug-loaded coating group. This study proved that drug-loaded ceramic-coated 3D-printed Mg alloy scaffolds have great application prospects in the field of medical implants and provided a new method for theoretical research and clinical treatment of functional material repair in osteoporotic bone defect repair.

## Acknowledgments

None.

## Funding

The authors thank the funding support from the National Key R&D Program of China (2022YFC2406000, subproject 2022YFC2406003), General program of National Natural Science Foundation of China (81972058, 82202680) and

Shanghai Municipal Key Clinical Specialty–Biomedical Materials (shslczdzk06701), 3-year Action Plan of Shenkang Development Center (SHDC2020CR2019B, SHDC2020CR6006-002), Huangpu District Industrial Support Fund (XK2020009) and National Key Science and Technology Infrastructure of Translational Medicine (Shanghai) Open Project (TMSZ-2020-207), Science and Technology Commission of Shanghai Municipality (22YF1422900), Shanghai Engineering Research Center of Innovative Orthopedic Instruments and Personalized Medicine (19DZ2250200), Shanghai Science and Technology Commission Yangtze River Delta Science and Technology Innovation Community Project (21002411200), Key R&D Programs of Ningxia, China (2020BCH01001, 2021BEG02037), and Technical Standard Project of Shanghai Science and Technology Commission (21DZ2201500).

## Conflict of interest

The authors declare no conflict of interest..

## Author contributions

*Conceptualization:* Zhaoyang Ran, Yongqiang Hao

*Investigation:* Zhaoyang Ran, Yan Wang, Jiaxin Li, Wenyu Xu, Jia Tan, Bojun Cao, Dinghao Luo, Yiwen Ding, Junxiang Wu, Lei Wang, Kai Xie, Liang Deng, Penghuai Fu, Xiaoying Sun, Liyi Shi, Yongqiang Hao

*Methodology:* Zhaoyang Ran, Yan Wang, Jiaxin Li

*Formal analysis:* Liang Deng, Kai Xie

*Writing – original draft:* Zhaoyang Ran

*Writing – review & editing:* Zhaoyang Ran, Liang Deng, Yongqiang Hao

## Ethics approval and consent to participate

This study was approved by the Ethics Committee of the Ninth People's Hospital, Shanghai Jiao Tong University School of Medicine (SH9H-2019-A668-1).

## Consent for publication

Not applicable.

## Availability of data

Data can be obtained from corresponding author on reasonable request.

## References

1. Johnell O, Kanis JA, 2006, An estimate of the worldwide prevalence and disability associated with osteoporotic fractures. *Osteoporos Int*, 17(12): 1726–1733.  
<https://doi.org/10.1007/s00198-006-0172-4>



2. Reid IR, 2020, A broader strategy for osteoporosis interventions. *Nat Rev Endocrinol*, 16(6): 333–339.  
<https://doi.org/10.1038/s41574-020-0339-7>
3. Myeroff C, Archdeacon M, 2011, Autogenous bone graft: Donor sites and techniques. *J Bone Joint Surg Am*, 93(23): 2227–2236.  
<https://doi.org/10.2106/JBJS.J.01513>
4. Sukotjo C, Lima-Neto TJ, Santiago Junior JF, *et al.*, 2020, Is there a role for absorbable metals in surgery? A systematic review and meta-analysis of Mg/Mg alloy based implants. *Materials (Basel)*, 13(18): 3914.  
<https://doi.org/10.3390/ma13183914>
5. John AA, Xie J, Yang YS, *et al.*, 2022, AAV-mediated delivery of osteoblast/osteoclast-regulating miRNAs for osteoporosis therapy. *Mol Ther Nucleic Acids*, 29: 296–311.  
<https://doi.org/10.1016/j.omtn.2022.07.008>
6. Kraus T, Fischerauer SF, Hanzl AC, *et al.*, 2012, Magnesium alloys for temporary implants in osteosynthesis: In vivo studies of their degradation and interaction with bone. *Acta Biomater*, 8(3): 1230–1238.  
<https://doi.org/10.1016/j.actbio.2011.11.008>
7. Min S, Wang C, Liu B, *et al.*, 2023, The biological properties of 3D-printed degradable magnesium alloy WE43 porous scaffolds via the oxidative heat strategy. *Int J Bioprint*, 9(3): 94–104.  
<https://doi.org/10.18063/ijb.686>
8. Chaya A, Yoshizawa S, Verdelis K, *et al.*, 2015, In vivo study of magnesium plate and screw degradation and bone fracture healing. *Acta Biomater*, 18: 262–269.  
<https://doi.org/10.1016/j.actbio.2015.02.010>
9. Li Y, Zhou J, Pavanram P, *et al.*, 2018, Additively manufactured biodegradable porous magnesium. *Acta Biomater*, 67: 378–392.  
<https://doi.org/10.1016/j.actbio.2017.12.008>
10. Dong J, Li Y, Lin P, *et al.*, 2020, Solvent-cast 3D printing of magnesium scaffolds. *Acta Biomater*, 114: 497–514.  
<https://doi.org/10.1016/j.actbio.2020.08.002>
11. Al-Ketan O, Rowshan R, Abu Al-Rub RK, 2018, Topology-mechanical property relationship of 3D printed strut, skeletal, and sheet based periodic metallic cellular materials. *Addit Manuf*, 19: 167–183.  
<https://doi.org/10.1016/j.addma.2017.12.006>
12. Zhang XY, Fang G, Zhou J, 2017, Additively manufactured scaffolds for bone tissue engineering and the prediction of their mechanical behavior: A review. *Materials*, 10(1): 50.  
<https://doi.org/10.3390/ma10010050>
13. Xie K, Wang NQ, Guo Y, *et al.*, 2022, Additively manufactured biodegradable porous magnesium implants for elimination of implant-related infections: An in vitro and in vivo study. *Bioact Mater*, 8: 140–152.  
<https://doi.org/10.1016/j.bioactmat.2021.06.032>
14. Rossi S, Deflorian F, Fedel M, 2019, Polysilazane-based coatings: Corrosion protection and anti-graffiti properties(dagger). *Surf Eng*, 35(4): 343–350.  
<https://doi.org/10.1080/02670844.2018.1465748>
15. Reid IR, Billington EO, 2022, Drug therapy for osteoporosis in older adults. *Lancet*, 399(10329): 1080–1092.  
[https://doi.org/10.1016/S0140-6736\(21\)02646-5](https://doi.org/10.1016/S0140-6736(21)02646-5)
16. Johnston CB, Dagar M, 2020, Osteoporosis in older adults. *Med Clin North Am*, 104(5): 873–884.  
<https://doi.org/10.1016/j.mcna.2020.06.004>
17. Black DM, Delmas PD, Eastell R, *et al.*, 2007, Once-yearly zoledronic acid for treatment of postmenopausal osteoporosis. *N Engl J Med*, 356(18): 1809–1822.  
<https://doi.org/10.1056/NEJMoa067312>
18. Li GY, Zhang L, Wang L, *et al.*, 2018, Dual modulation of bone formation and resorption with zoledronic acid-loaded biodegradable magnesium alloy implants improves osteoporotic fracture healing: An in vitro and in vivo study. *Acta Biomater*, 65: 486–500.  
<https://doi.org/10.1016/j.actbio.2017.10.033>
19. Liu A, Lin D, Zhao H, *et al.*, 2021, Optimized BMSC-derived osteoinductive exosomes immobilized in hierarchical scaffold via lyophilization for bone repair through Bmpr2/Acyr2b competitive receptor-activated Smad pathway. *Biomaterials*, 272: 120718.  
<https://doi.org/10.1016/j.biomaterials.2021.120718>
20. Yuan K, Mei J, Shao D, *et al.*, 2020, Cerium oxide nanoparticles regulate osteoclast differentiation bidirectionally by modulating the cellular production of reactive oxygen species. *Int J Nanomed*, 15: 6355–6372.  
<https://doi.org/10.2147/IJN.S257741>
21. Chen QX, Li JY, Han F, *et al.*, 2022, A multifunctional composite hydrogel that rescues the ROS microenvironment and guides the immune response for repair of osteoporotic bone defects. *Adv Func Mater*, 32(27): 2201067.  
<https://doi.org/10.1002/adfm.202201067>
22. Niu J, Yuan G, Liao Y, *et al.*, 2013, Enhanced biocorrosion resistance and biocompatibility of degradable Mg-Nd-Zn-Zr alloy by brushite coating. *Mater Sci Eng C Mater Biol Appl*, 33(8): 4833–4841.  
<https://doi.org/10.1016/j.msec.2013.08.008>
23. Lin ZJ, Wu J, Qiao W, *et al.*, 2018, Precisely controlled delivery of magnesium ions thru sponge-like monodisperse



- PLGA/nano-MgO-alginate core-shell microsphere device to enable in-situ bone regeneration. *Biomaterials*, 174: 1–16.  
<https://doi.org/10.1016/j.biomaterials.2018.05.011>
24. Zhai Z, Qu X, Li H, *et al.*, 2014, The effect of metallic magnesium degradation products on osteoclast-induced osteolysis and attenuation of NF-kappaB and NFATc1 signaling. *Biomaterials*, 35(24): 6299–6310.  
<https://doi.org/10.1016/j.biomaterials.2014.04.044>
25. Wong HM, Wu SL, Chu PK, *et al.*, 2013, Low-modulus Mg/PCL hybrid bone substitute for osteoporotic fracture fixation. *Biomaterials*, 34(29): 7016–7032.  
<https://doi.org/10.1016/j.biomaterials.2013.05.062>
26. Lin SH, Yang GZ, Jiang F, *et al.*, 2019, A magnesium-enriched 3D culture system that mimics the bone development microenvironment for vascularized bone regeneration. *Adv Sci*, 6(12): 1900209.  
<https://doi.org/10.1002/advs.201900209>
27. Cipriano AF, Lin JJ, Lin A, *et al.*, 2017, Degradation of bioresorbable Mg-4Zn-1Sr intramedullary pins and associated biological responses in vitro and in vivo. *ACS Appl Mater Interfaces*, 9(51): 44332–44355.  
<https://doi.org/10.1021/acsami.7b15975>
28. Zhang YL, Shi LT, Tang PF, *et al.*, 2017, Comparison of the efficacy between two micro-operative therapies of old patients with osteoporotic vertebral compression fracture: A network meta-analysis. *J Cell Biochem*, 118(10): 3205–3212.  
<https://doi.org/10.1002/jcb.25966>
29. Reid DM, Devogelaer JP, Saag K, *et al.*, 2009, Zoledronic acid and risedronate in the prevention and treatment of glucocorticoid-induced osteoporosis (HORIZON): A multicentre, double-blind, double-dummy, randomised controlled trial. *Lancet*, 373(9671): 1253–1263.  
[https://doi.org/10.1016/S0140-6736\(09\)60250-6](https://doi.org/10.1016/S0140-6736(09)60250-6)
30. Greiner S, Kadow-Romacker A, Schmidmaier G, *et al.*, 2009, Cocultures of osteoblasts and osteoclasts are influenced by local application of zoledronic acid incorporated in a poly(D,L-lactide) implant coating. *J Biomed Mater Res A*, 91(1): 288–295.  
<https://doi.org/10.1002/jbm.a.32245>
31. Razavi M, Fathi M, Savabi O, *et al.*, 2014, In vivo study of nanostructured diopside (CaMgSi<sub>2</sub>O<sub>6</sub>) coating on magnesium alloy as biodegradable orthopedic implants. *Appl Surf Sci*, 313: 60–66.  
<https://doi.org/10.1016/j.apsusc.2014.05.130>
32. Yang M, Dong Y, He Q, *et al.*, 2020, Hydrogen: A novel option in human disease treatment. *Oxid Med Cell Longev*, 2020: 8384742.  
<https://doi.org/10.1155/2020/8384742>
33. Ohta S, 2014, Molecular hydrogen as a preventive and therapeutic medical gas: Initiation, development and potential of hydrogen medicine. *Pharmacol Therapeut*, 144(1): 1–11.  
<https://doi.org/10.1016/j.pharmthera.2014.04.006>